A Case Study of Airmass Transformation and Cloud Formation at Summit, Greenland

AMY SOLOMON AND MATTHEW D. SHUPE

Cooperative Institute for Research in Environmental Sciences, University of Colorado Boulder, and NOAA/ESRL/PSD, Boulder, Colorado

(Manuscript received 6 March 2019, in final form 26 June 2019)

ABSTRACT

This study investigates cloud formation and transitions in cloud types at Summit, Greenland, during 16–22 September 2010, when a warm, moist air mass was advected to Greenland from lower latitudes. During this period there was a sharp transition between high ice clouds and the formation of a lower stratocumulus deck at Summit. A regional mesoscale model is used to investigate the air masses that form these cloud systems. It is found that the high ice clouds form in originally warm, moist air masses that radiatively cool while being transported to Summit. A sensitivity study removing high ice clouds demonstrates that the primary impact of these clouds at Summit is to reduce cloud liquid water embedded within the ice cloud and water vapor in the boundary layer due to vapor deposition on snow. The mixed-phase stratocumulus clouds form at the base of cold, dry air masses advected from the northwest above 4 km. The net surface radiative fluxes during the stratocumulus period are at least 20 W m^{-2} larger than during the ice cloud period, indicating that, in seasons other than summer, cold, dry air masses advected to Summit above the boundary layer may radiatively warm the top of the Greenland Ice Sheet more effectively than warm, moist air masses advected from lower latitudes.

1. Introduction and motivation

Understanding how changes in large-scale circulation patterns impact the Greenland Ice Sheet (GrIS) requires an understanding of how air masses are modified as they are advected over the GrIS. For example, during North Atlantic blocking events, air masses advected northward are warmed and moistened by fluxes from the ocean before they are advected over the GrIS. The rising air masses cool causing cloud ice and/or cloud liquid to form and snow and/or rain to fall on the GrIS. Summit Station (hereafter Summit) is an observatory located at the top of the GrIS at 72°36′N, 38°25′W and an elevation of 3216 m. The processes that modify the air masses along the trajectories to Summit determine the phase of the clouds, and therefore the radiative fluxes, precipitation, cloud-driven mixing, and turbulent fluxes that impact the surface energy and mass budgets of the GrIS. Understanding the role these air masses play in the GrIS climate requires accurate models of the timing, location, spatial organization, and phase of cloud and precipitation processes.

The North Atlantic Oscillation Index (NAO) is a measure of the surface pressure difference between the subtropical Azores high and the subpolar Icelandic low (Walker and Bliss 1932) and is the dominant mode of atmospheric variability over the North Atlantic Ocean (Wallace and Gutzler 1981; Hurrell 1995). The NAO index is associated with changes in the intensity and location of the North Atlantic jet stream and storm track, and attendant fluxes of heat and moisture (Thompson et al. 2002; Vallis and Gerber 2008; Woollings et al. 2010; Hall et al. 2015). A negative NAO pattern is typically associated with a persistent high pressure system (or "blocking" system) over the Greenland–Iceland region, due to cyclonic wave breaking events, that causes warm air to be advected into northeastern Canada and Greenland and cold air to be advected into western Europe (Benedict et al. 2004; Franzke et al. 2004; Strong and Magnusdottir 2008).

The NAO pattern is strongly anticorrelated with the Greenland blocking index (GBI; Woollings et al. 2008; Davini et al. 2012; Hanna et al. 2015), which is a measure of the low-frequency teleconnections that cause anomalous fluxes of heat and momentum into the Greenland region. The GBI is defined as the mean 500 hPa geopotential height averaged over 60°–80°N, 20°–80°W (Fang 2004). Since 1991, the GBI has been significantly increasing in all seasons, with largest increases in

Corresponding author: Amy Solomon, amy.solomon@noaa.gov

DOI: 10.1175/JAS-D-19-0056.1

summer and winter (Hanna et al. 2013, 2018). However, correlations of the melt fraction from the Moderate Resolution Imaging Spectroradiometer from the *Terra* and *Aqua* satellites with atmospheric circulation patterns indicate that even though the number of melt days is correlated with locally defined blocking events (Häkkinen et al. 2014), they are only weakly correlated with the NAO and GBI, indicating other significant atmospheric circulation patterns and local conditions that influence melt (Välisuo et al. 2018). For example, the east Atlantic circulation pattern, can amplify or weaken blocking events during strong negative NAO periods (Lim et al. 2016). In addition, anomalous regions of sea ice loss can impact the spatial structure of the NAO and attendant fluxes of heat and moisture into the Greenland region (Pedersen et al. 2016), which impacts cloud phase and cloud feedbacks over the GrIS.

The challenge and significance of adequately simulating cloud and precipitation processes associated with advection from lower latitudes to the polar regions was clearly demonstrated in studies of the 2012 extreme GrIS melt event, when over 98% of the GrIS surface was observed to experience melt (Nghiem et al. 2012; Hanna et al. 2014; Neff et al. 2014). Energy balance and mesoscale limited-area models demonstrate that this melt would not have occurred over such a large spatial extent without the additional warming of the surface due to radiative fluxes from low-level, thin liquid-bearing stratocumulus (Bennartz et al. 2013; Solomon et al. 2017). These cloud systems are notoriously difficult to model, due to the challenge of maintaining cloud liquid in models in the presence of cloud ice (Klein et al. 2009; Morrison et al. 2009b; Solomon et al. 2009). Another modeling challenge is adequately representing precipitation processes, since these processes compose the primary mass input of these cloud systems to the GrIS mass budget and control the longevity of cloud systems.

In this study we use a mesoscale regional atmosphere–land model to study airmass modification and cloud formation at Summit during September 2010 when a large suite of instruments measured the atmosphere, precipitation, clouds, and surface conditions at the top of the GrIS at Summit Station during the Integrated Characterization of Energy, Clouds, Atmospheric State and Precipitation at Summit (ICECAPS) project (see Shupe et al. 2013). This period was unique due to its presence within the longest period of sustained negative 3-month running-mean NAO indices since 1950 (http://www.cpc.ncep.noaa.gov/products/precip/CWlink/pna/nao.shtml).

We investigate how advection of heat and moisture from lower latitudes in autumn impacts cloud formation and transitions in cloud types at Summit, Greenland. We identify to what extent these cloud systems can be represented in the state-of-the-art European Centre for Medium-Range Weather Forecasts (ECMWF; see European Centre for Medium-Range Weather Forecasts 2009) interim reanalyses (ERA-Interim) and demonstrate that low-level stratocumulus are frequently not simulated at Summit in ERA-Interim, consistent with the underrepresentation of observed boundary layer inversions. We then use tracer studies to identify how air masses are modified through mixing, cloud formation, and precipitation processes as they are advected to Summit and demonstrate a methodology for understanding how air masses evolve and interact, a methodology that could be potentially expanded to longer-term analyses.

2. Observed conditions during 16–22 September 2010

Model simulations are validated with observations taken at Summit Station from the ICECAPS project, which has been measuring atmospheric, cloud, and precipitation properties at Summit since May 2010. Summit is at 3216 m above sea level. All heights in this paper are relative to sea level. Pressure, temperature, and relative humidity measurements from twice-daily radiosondes are used to validate the atmospheric structure.

Radar reflectivity and mean Doppler velocity from a Doppler 35-GHz millimeter cloud radar (MMCR; Moran et al. 1998) are used (along with the CR-SIM cloud radar simulator) to validate the mass and vertical motions of frozen hydrometers. A cloud-type classification that uses cloud radar, depolarization lidar, microwave radiometer, and temperature soundings developed by Shupe (2007) is used to identify liquid and cloud layers.

This study is focused on 16–22 September 2010 at Summit. During this time, high ice clouds (up to 10 km) were observed from 17 to 19 September 2010 (Fig. 1a). Liquid layers are periodically embedded within the ice cloud (Fig. 1b). At the end of 18 September 2010 there was a rapid transition from high ice clouds to low-level mixed-phase stratocumulus clouds that slowly descended from 5.8 to 4.2 km and persisted until the middle of 21 September 2010. Even though ice mass variability can be seen in the stratocumulus cloud, the radar reflectivity is more uniform than in the ice cloud, with radar reflectivities generally above −15 dBZ. From hereon, 17–19 September will be referred to as the "ice cloud period" and 19–21 September will be referred to as the "mixed-phase stratocumulus period."

The larger-scale context for this case involves a warm and moist air mass advected into the Greenland region from the North Atlantic (Fig. 2). At the start of the analysis period at 0000 UTC 16 September 2010, the air mass on the 296 K constant potential temperature surface, or isentrope, at the southern tip of Greenland is 2 km high with a temperature ~277 K and specific

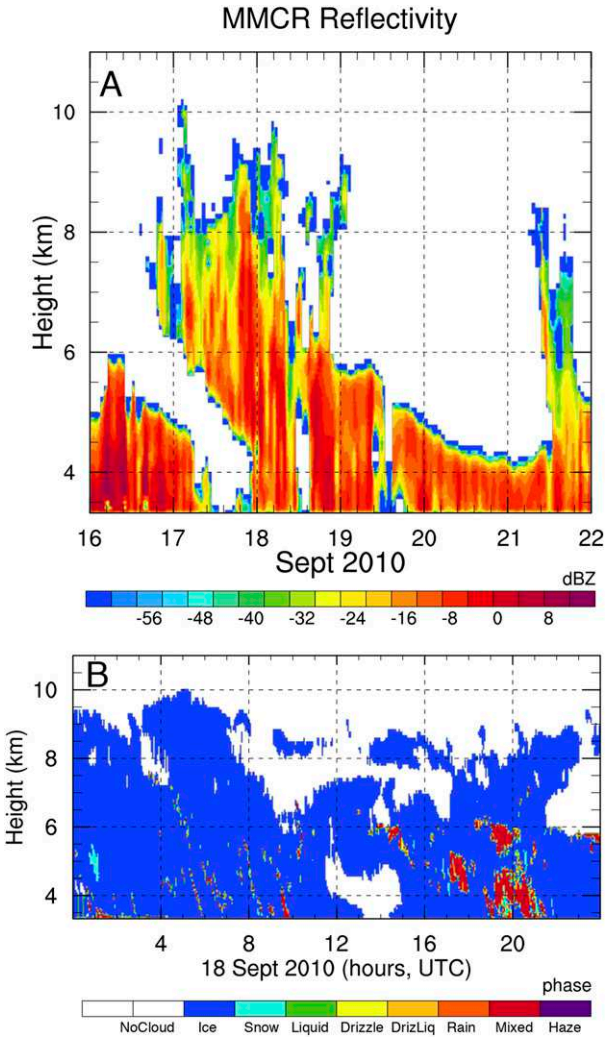

FIG. 1. (a) Summit MMCR 10-min averaged radar reflectivity (interpolated to hourly values; dBZ) for 16–22 Sep 2010. Height is with respect to sea level. (b) Observed cloud phase on 18 Sep 2010. Height is with respect to sea level.

humidity greater than 5 g kg^{-1}. This is the isentrope that intersects the mixed-phase cloud top observed at Summit on 20 September and helps us to estimate the horizontal motion of the air mass in the absence of diabatic processes or cross-isentropic mixing. Note that the air on this isentrope in the northwest of Greenland has a frozen moist static energy (MSE; defined in section 3) that is 10 K higher than in southern Greenland, an indication of airmass modification due to moist diabatic processes and/or different airmass sources.

3. Model setup and experiment design

The Weather Research and Forecasting (WRF) Model, version 3.6.1 (Skamarock et al. 2008), is used for this study with a 3000 km × 3000 km horizontal domain (shown in Fig. 2) with grid spacing of 24 km in the horizontal and 128 (x) × 128 (y) × 110 (z) grid points. The WRF with Chemistry (WRF-CHEM) subroutines are used so that passive tracers are vertically mixed by subgrid turbulence and cumulus convection and can be tracked in space and time. The boundary layer is well resolved in the vertical by including 28 levels in the lowest 1 km. The model is forced with lateral and surface boundary conditions from the 6-hourly, T255 ERA-Interim dataset. The model is spun up by integrating from 0000 UTC 14 September to 0000 UTC 16 September 2010. For the analysis, 16–22 September 2010 is used. Gridpoint nudging to the ERA-Interim temperature, winds, and specific humidity above 400 hPa (above ~7 km) is used to constrain the large-scale flow and to allow the boundary layer to evolve without constraints.

The WRF configuration uses the National Center for Atmospheric Research Community Atmospheric Model longwave and shortwave radiation package, where the longwave code allows for interactions with resolved clouds and cloud fractions (Collins et al. 2004). Boundary layer mixing is parameterized with the Grenier–Bretherton–McCaa scheme, which uses a 1.5-order turbulent closure model with an entrainment closure at the boundary layer top and has been tested for cloud-topped boundary layers (Grenier and Bretherton 2001). The surface layer is parameterized with the revised MM5 surface-layer scheme, which includes modifications to provide more suitable similarity functions to simulate the surface-layer evolution under strong stable/unstable conditions (Jimenez et al. 2012). The National Center for Atmospheric Research Community Land Model, version 4 (CLM4), is used to simulate the ice sheet and surrounding land surfaces (Lawrence et al. 2011). The CLM4 uses up to 5 layers for the snowpack and 10 layers for the soil and ice sheet. The ice sheet mass balance can change through snow accumulation and melt, water transfer between snow layers, infiltration, evaporation, surface runoff, and subsurface drainage. This scheme uses the Snow, Ice, and Aerosol Radiative Model (SNICAR) to calculate snow albedo and solar absorption within each snow layer. This combination of CLM4–SNICAR has been shown to well represent the temporal and spatial variability of surface albedo over the GrIS (Solomon et al. 2017).

Microphysics is simulated with the Morrison two-moment scheme, which includes prognostic equations for mixing ratio and number concentration for cloud droplets, cloud ice, rain, snow, and graupel/hail. Cloud ice is initiated by immersion freezing for temperatures greater than −40°C and by homogeneous nucleation for temperatures less than −40°C. Also, a parameterization for cirrus cloud formation has been added to the model due to observations

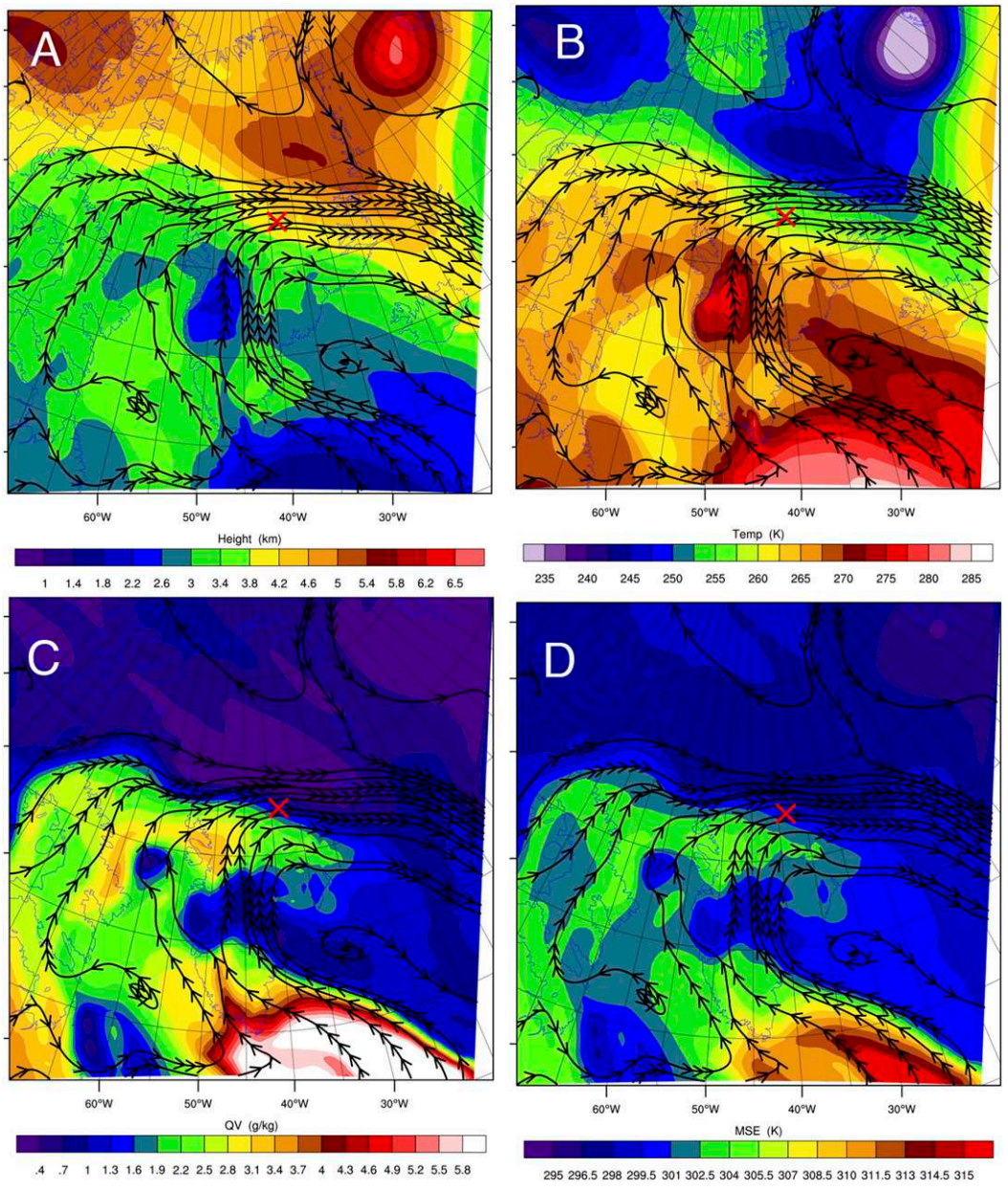

FIG. 2. Streamlines, (a) height (km), (b) temperature (K), (c) specific humidity (g kg^{-1}), and (d) MSE (K) on the 296-K isentrope at 0000 UTC 16 Sep 2010 from ERA-Interim. The 296-K isentrope intersects the mixed-phase cloud top at Summit on 20 Sep. Red crosses mark the location of Summit. Coastlines are indicated with thin blue lines.

at Summit that indicate cloud ice can form in the absence of cloud droplets. However, adding this parameterization had a negligible impact on the simulations. Cloud droplets are activated in regions of low cloud water content using resolved and subgrid vertical motion (Morrison and Pinto 2005) and a lognormal aerosol size distribution to derive cloud condensation nuclei spectra following Abdul-Razzak and Ghan (2000). The lognormal dry aerosol size distribution is given by

$$\frac{dN}{d\ln r} = \frac{N_t}{\sqrt{2\pi}\ln\sigma}\exp\left[\frac{\ln^2\left(\frac{r}{r_m}\right)}{2\ln^2\sigma}\right], \qquad (1)$$

where N is the number concentration of aerosols and r is the particle radius. The parameters N^t, r^m, and σ are total number concentration, geometric-mean radius, and

standard deviation of the particle mode, and are given the values $30\,\mathrm{cm}^{-3}$, $0.188\,\mu\mathrm{m}$, and 1.4, respectively, based on CCN measurements made at Summit by A. Nenes et al. (2017, personal communication). Aerosol composition is assumed to be 30% insoluble by volume, with the remaining soluble component consisting of ammonium bisulfate. Morrison et al. (2009a) and Morrison and Pinto (2005) provide details of the parameterizations used in this microphysical scheme.

A radar simulator is used to consistently compare the model results to the radar measurements. The simulator (CR-SIM) was developed by the McGill University Clouds Research Group (radarscience.weebly.com) and is freely available to the public. It uses input from the WRF Model and can be setup to take into account all microphysical options used to produce the model simulations, the modeled atmospheric turbulent state, and the specific characteristics of the cloud radar.

We use frozen MSE to identify how air masses are modified as they are advected to Summit. MSE is approximately conserved during moist adiabatic processes and calculated as

$$\mathrm{MSE} = c_p T + L_v q_v + gZ - L_f q_i, \qquad (2)$$

where c_p is the specific heat of dry air at constant pressure, T is temperature, L_v is the latent heat of vaporization, q_v is the water vapor mixing ratio, g is the acceleration of gravity, L_f is the latent heat of fusion, q_i is the total ice water mixing ratio, and Z is the geopotential height. MSE is conserved in the absence of surface fluxes, radiative heating/cooling, and turbulent mixing. Following a tracer trajectory, the moist static energy tendency is written as

$$\frac{d}{dt}\mathrm{MSE} = \mathrm{LW} + \mathrm{SW} + \mathrm{SH} + \mathrm{LH} + \mathrm{MIX}, \qquad (3)$$

where LW is the longwave radiative heating rate, SW is the shortwave radiative heating rate, SH is the surface sensible heat flux, LH is the surface latent heat flux, and MIX is subgrid-scale turbulent mixing.

Tracers are used to tag air masses coming from a specified column of air by distinguishing them into eight categories based on their MSE at 0000 UTC 14 September 2010 and set to one in the column every time step. This creates a tracer plume emanating from the column.

Processes that cause airmass transformation can be isolated by tracing the advected air masses backward in time. This is done by tracking the location of the maximum tracer concentration backward in time starting at Summit at a specified height to the initial location of the air mass at the start of the simulations (0000 UTC 14 September 2010). Once the primary trajectories are isolated, the approximate Lagrangian airmass properties can be calculated from the initial location along the trajectory to Summit. Tendencies along the trajectory can be calculated taking the large-scale vertical motion into account.

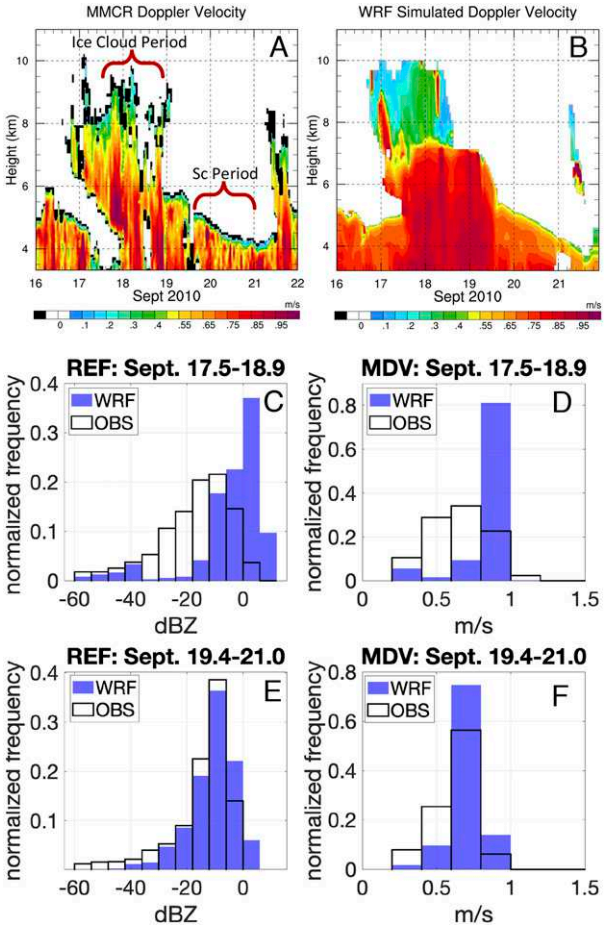

FIG. 3. Comparison of 10-min averaged MMCR Doppler velocity ($\mathrm{m\,s}^{-1}$) and reflectivity (dBZ) (interpolated to hourly values) to hourly WRF simulated fields at Summit. (a) Time–height cross section of MMCR Doppler velocity. Ice cloud and stratocumulus periods used to form histograms are indicated with brackets. (b) Time–height cross section of WRF simulated Doppler velocity. (c) Histogram of reflectivity during ice cloud period (17.5–18.9 Sep). Observations are shown with black lines; model results are shown with solid blue bars. (d) Histogram of Doppler velocity during ice cloud period (17.5–18.9 Sep). (e) Histogram of radar reflectivity during stratocumulus period (19.6–21 Sep). (f) Histogram of Doppler velocity during stratocumulus period (19.6–21 Sep) Height is with respect to sea level.

4. Results

a. *Validation with ICECAPS measurements*

The CR-SIM radar simulator is used to compare the simulated hourly cloud properties at Summit to MMCR cloud radar observations (Fig. 3). Figures 3a and 3b show the close structural correspondence in space and

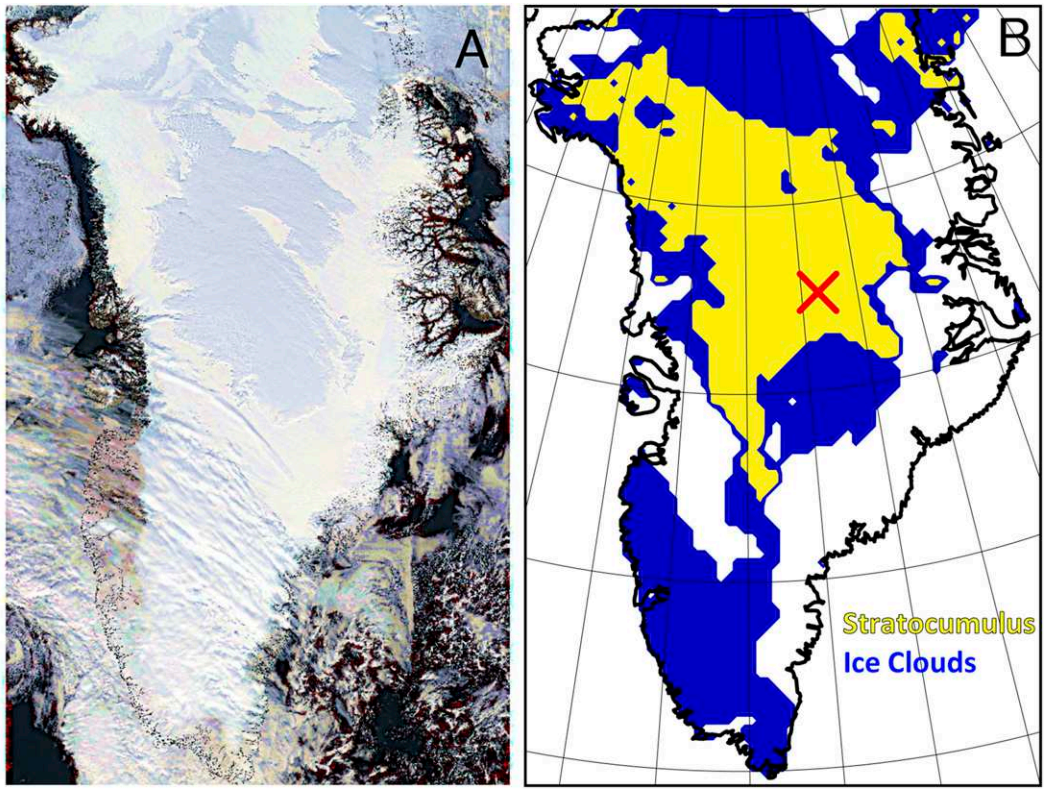

FIG. 4. Comparison of (a) *Terra* MODIS true-color image of Greenland on 20 Sep 2010 and (b) cloud mask of WRF simulation at 0700 UTC 20 Sep 2010. Summit is marked with a red cross in (b). The cloud mask indicates cloud liquid water with cloud ice and snow below in yellow and cloud ice without any cloud liquid above in blue.

time of measured and simulated Doppler velocity at Summit for 16–22 September 2010, even though the simulation is started at 0000 UTC 14 September 2010 and the nudging is only applied above 10 km. This highlights the controlling influence of the air masses above 7.5 km on the structure and timing of the high ice clouds and the transition to the stratocumulus period. The transition to a stratocumulus cloud occurs at about the right time but is 1 km too high on 19 September relative to the MMCR measurements. This error is due to starting the simulation five days before the stratocumulus period (as demonstrated by simulations started on 16 and 18 September), but starting so early is necessary to produce airmass source regions near the Greenland coastlines for these events.

Mean Doppler velocities are estimates of ice fall speeds plus vertical air motions. In the ice cloud the Doppler velocities are observed to increase from $\sim 0.2\,\mathrm{m\,s^{-1}}$ at 9 km to $\sim 0.7\,\mathrm{m\,s^{-1}}$ below 6 km as particles grow when they fall. Up and down drafts with shafts of high and low velocities are clearly seen every 1–2 h. Observed ice motions are more pronounced in the stratocumulus cloud, as a result of shallow convection in these clouds, with Doppler velocities greater than $1\,\mathrm{m\,s^{-1}}$ in the downdrafts and close to zero in the updrafts. The simulated Doppler velocities are within the range of measurements but more uniform due to the resolution of the model, both in the ice and stratocumulus clouds. Figures 3c–f show histograms of radar reflectivity (Figs. 3c,e) and mean Doppler velocity (Figs. 3d,f) for the two different periods. During the stratocumulus period the model correspondence is striking, showing only a small tendency to underestimate the periods of smallest ice mass, likely related to differences in spatial resolution. For the ice period, while the modeled range overlaps the observed range, the model does not well capture the intermediate ice masses and generally overestimates both reflectivity and mean Doppler velocity, suggesting that modeled ice particles are often too large.

Satellite imagery of the stratocumulus period on 20 September 2010 (Fig. 4a) shows stratocumulus clouds covering the top of the GrIS with thin banded ice clouds covering the southern tip below 68.5°N. A cloud mask of modeled cloud properties over the GrIS at 0700 UTC 20 September 2010 (Fig. 4b) shows a similar pattern of cloud systems. The modeled stratocumulus clouds extend too far north compared to the satellite image and the ice clouds in the south are not as extensive as the

observations; otherwise, the model is able to simulate the observed horizontal cloud structure at this time.

The simulated atmospheric temperature and relative humidity at Summit during the ice cloud and stratocumulus periods compared to radiosondes and the ERA-Interim used to initialize and nudge the simulation is shown in Fig. 5. The simulated atmospheric structure during the ice cloud period deviates from the sounding between 7 and 8 km, where relative humidity is observed to be low, and at the surface, where a ~10-K surface inversion is observed, but the high air mass (above 8 km) that produces the ice cloud is well simulated. The ERA-Interim field also fails to represent the dry air mass between 7 and 8 km but has smaller temperatures biases below 7 km than the simulation. It is important to note that the Summit radiosondes were not available on the global telecommunication system for assimilation into ERA-Interim during this period.

The simulated atmospheric structure during the stratocumulus period closely approximates the sounding except that features such as the high relative humidity at 10 km and the stratocumulus clouds at 5 km are displaced vertically by 0.5 km. Interestingly, the simulation is able to produce the layered cloud and boundary layer structure up to 2 km above the surface, while ERA-Interim is not. This is generally the case at Summit, with only 1% of the observed boundary layer inversions represented in ERA-Interim based on twice daily soundings at Summit between June 2010 and December 2013 (results not shown). This illustrates the motivation for constraining the large-scale circulation with the ERA-Interim fields above the tropopause and allowing the model physics to determine the cloud and boundary layer structure. Furthermore, this demonstrates the broader difficulty in using reanalyses like ERA-Interim to understand the interaction of stratocumulus (i.e., liquid containing) clouds with the GrIS surface.

b. *Tracer study*

Passive tracers are used in this study to track the evolution of air masses that form ice and stratocumulus clouds at Summit. A series of simulations were run to find where air masses that make up the ice clouds and stratocumulus clouds at Summit originate. It was found that tracers starting on 0000 UTC 14 September in two 240 km × 360 km regions are responsible for the majority of the air below 10 km at Summit during 18–21.5 September. These two regions are the southwest (Fig. 6a) and northwest coasts of Greenland (Fig. 6b).

To identify how the air masses from these two regions are modified as they are advected to Summit, each region is tagged with eight passive tracers using MSE intervals: in the northwest, less than 298, 298–301, 301–304, 304–306, 306–308, 308–310, 310–312, and greater than 312 K; in the southwest; less than 296, 296–298, 298–300, 300–302, 302–304, 304–306, 306–308, and greater than 308 K. In addition, two model runs were done to identify if air masses within the atmospheric boundary layer away from the

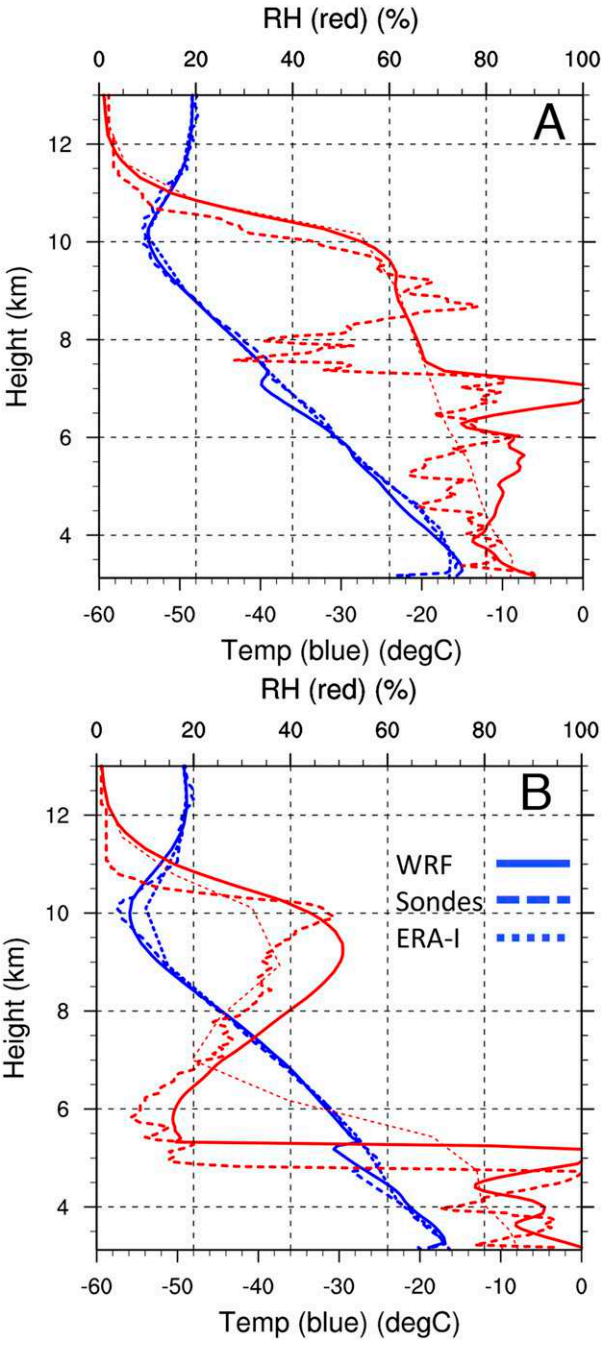

FIG. 5. Comparison of simulated atmospheric temperatures (solid blue lines; °C) and relative humidity (solid red lines; %) at Summit to radiosondes (dashed lines) and ERA-Interim (dotted lines) at (a) 1200 UTC 18 Sep and (b) 0000 UTC 20 Sep 2010. Height is relative to sea level.

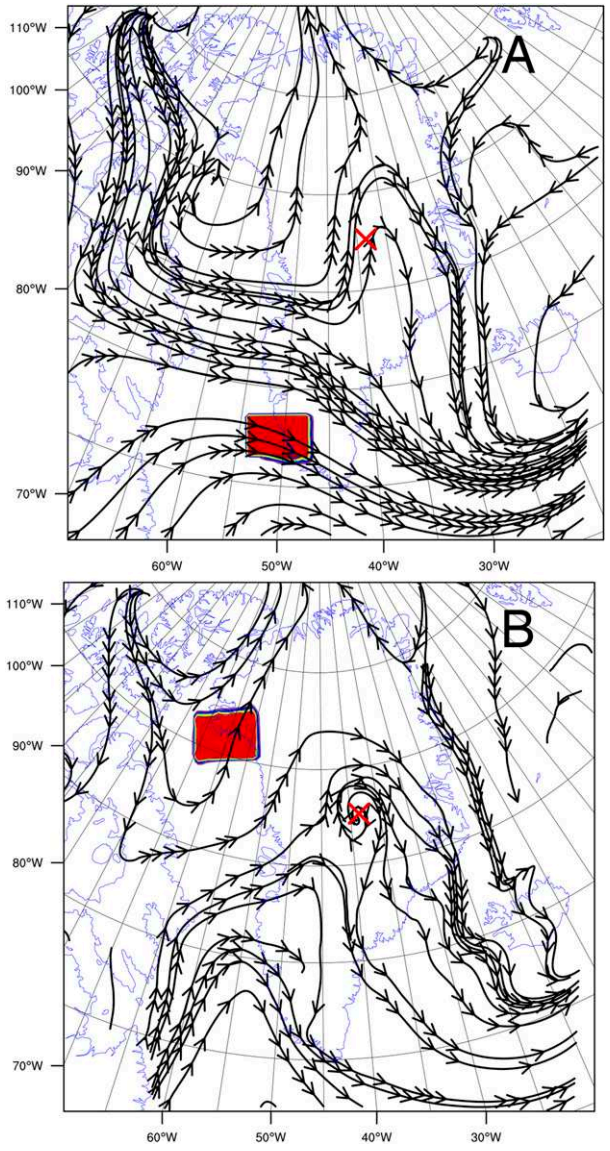

FIG. 6. Tracer location at 0100 UTC 14 Sep 2010 (red boxes) and streamlines on specified MSE surface. Tracer in these two locations makes up 100% of the air at Summit on Sep 20. (a) Tracer from south Greenland and streamlines on 310-K MSE (the MSE surface that intersect the ice cloud on 18 Sep). (b) Tracer northwest of Greenland and streamlines on 296-K MSE (the MSE surface that intersect the liquid cloud top on 20 Sep). Summit is marked with a red cross.

Greenland landmass reach Summit by setting a tracer equal to one within the boundary layer and a different tracer equal to one above the boundary layer everywhere in the domain except over Greenland. The tracers are set to one within these regions at every time step starting 0000 UTC 14 September 2010. This produces tracer plumes emanating from the regions in specified MSE ranges. These tracers show that air originating near the southwest coast of Greenland is advected up over the GrIS producing the high ice cloud (Figs. 6a and 7a) and air originating along the northwest coast of Greenland produces the stratocumulus cloud-top/inversion structure (Figs. 6b and 7b). The air mass below the inversion during the stratocumulus period is composed of approximately equal tracer concentrations from the southwest and northwest. The run with the atmospheric boundary layer tagged with a tracer away from the Greenland landmass shows that less than 10% of the air below the inversion originates in the boundary layer; this air is therefore advected into the domain above the boundary layer (results not shown).

The air mass that produces the ice cloud originally had MSE greater than 308 K but as the air mass moves up and over the GrIS to Summit the MSE is reduced by more than 6 K (Fig. 8a). Diagnostics to identify what causes the MSE to decrease are presented in the next section. For the stratocumulus period, the MSE of the air mass that produces the cloud-top/inversion properties is essentially unchanged from the initial values until it is mixed down into the boundary layer through cloud-top entrainment (Fig. 8b). The cold, dry air mass from the northwest (Figs. 8c,d) overlays moist air previously advected in from the south (Fig. 6a). The dry air mass at cloud top allows the cloud to radiate to space more efficiently, driving stronger turbulence that maintains cloud liquid water formation.

c. *Airmass transformation along tracer trajectories*

In this section we identify how air masses are modified as they are advected from the southwest coast of Greenland to Summit. We focus on two different tracers to examine which air masses reach Summit within the boundary layer (providing moisture for the stratocumulus clouds) and which air masses reach Summit above the boundary layer (forming the ice clouds). Two tracers are used to illustrate the evolution of these different air masses. The first is a tracer with initial MSE between 300 and 302 K (concentrations of this tracer at Summit are shown in Fig. 9a, referred to hereafter as S1). The second is a tracer with initial MSE between 306 and 308 K (concentrations at Summit shown in Fig. 9b, referred to hereafter as S2).

Air in the boundary layer at Summit below the stratocumulus deck is primarily composed of air masses advected in from south Greenland (Fig. 6a). Tracer S1 makes up over 25% of this air mass (Fig. 9a). At Summit in the region of maximum concentration the MSE is 2–5 K less than the initial MSE. To understand the evolution of the air mass to this point, we examine the processes modifying MSE along the airmass trajectory.

Trajectories are produced by following the location of the maximum tracer concentration from Summit

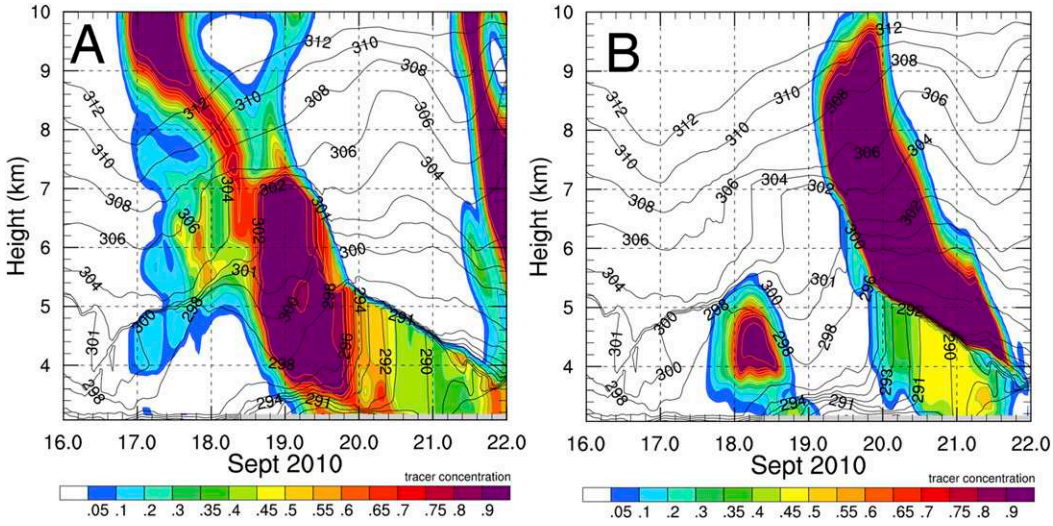

FIG. 7. Time–height cross sections of total (sum over all MSE intervals) tracer concentrations at Summit. Black contours are MSE. Tracers are initialized at 0000 UTC 14 Sep 2010. (a) Tracer from southwest (see Fig. 6a). (b) Tracer from northwest (see Fig. 6b). Height is with respect to sea level.

backward in time. The evolution of the air mass and changes in the airmass properties are then calculated by following the trajectory forward in time. The trajectory for tracer S1 given in Fig. 9a is shown in Fig. 10a. A time–height cross section of tracer concentration along the trajectory is shown in Fig. 10c. Tracer S1 originates 1–2 km above sea level off the Greenland coast in the Labrador Sea. The tracer does not extend before 16 September because before then the tracer from that location is advected southward out of the domain. MSE in S1 changes by less than 0.5 K from the coastline to the top of the GrIS (0000 UTC 17 September–0000 UTC 18 September); that is, there is a general cancellation between moist MSE changes and dry MSE changes: 4.5 K from changes in specific humidity due to precipitation and 4.5 K from changes in height and temperature. Snow continuously falls through the saturated air mass as the air mass moves to the top of the GrIS (Figs. 11a,c). It is interesting to note that high liquid cloud formation prevents the liquid clouds within the air mass from radiating efficiently to space (Fig. 11e); this would have significantly cooled the air mass by longwave cooling and produced cloud-driven mixing. The air mass with tracer concentration greater than 70% is saturated with respect to water between 17.1 and 17.6 September as it is lifted up onto the GrIS and subsaturated with respect to water after it reaches the top of the GrIS. As the air mass moves along the top of the GrIS, the relative humidity stays between 90% and 92% while the MSE decreases by 3 K (0000 UTC 18 September–0600 UTC 19 September), 1 K from a decrease in specific humidity due to precipitation and 1 K from a decrease in temperature, primarily due to subgrid mixing with drier air and nighttime longwave radiative cooling of the surface (Figs. 11a,c,e).

The trajectory for tracer S2 given in Fig. 9b is shown in Fig. 10b. A time–height cross section of tracer concentration along the trajectory is shown in Fig. 10d. Tracer S2 originates 5–6 km above sea level off the Greenland coast in the Labrador Sea to the west of the initial location of tracer S1. Tracer S2 follows a more direct trajectory to Summit and arrives at Summit without a change in height. From 0600 UTC 16 September to 0000 UTC 19 September, the MSE in S2 decreases by 4.5 K: 0.5 K from a decrease in specific humidity and 4 K from a decrease in temperature. A strong step change in the cooling of the air mass occurs due to the longwave cooling impact of liquid cloud formation at 5–7 km on 17–18 September. Snow continuously falls from the air mass without significantly reducing the water vapor mixing ratio within the trajectory.

d. Impact of high ice cloud on boundary layer and stratocumulus dynamics

A model sensitivity study was run to determine the impact of high ice clouds on boundary layer and stratocumulus evolution. The sensitivity study removed all frozen hydrometeors that form above 5.5 km after 1200 UTC 17 September. Air masses that form ice and stratocumulus clouds at Summit are not modified before 1200 UTC 17 September. The most significant impact of the high ice clouds is to limit the amount of cloud liquid that forms below (Figs. 12a,b). This reduces the cloud liquid water path (LWP) during times of ice shafts from 180 g m^{-2} to less than 20 g m^{-2} and increases the peak

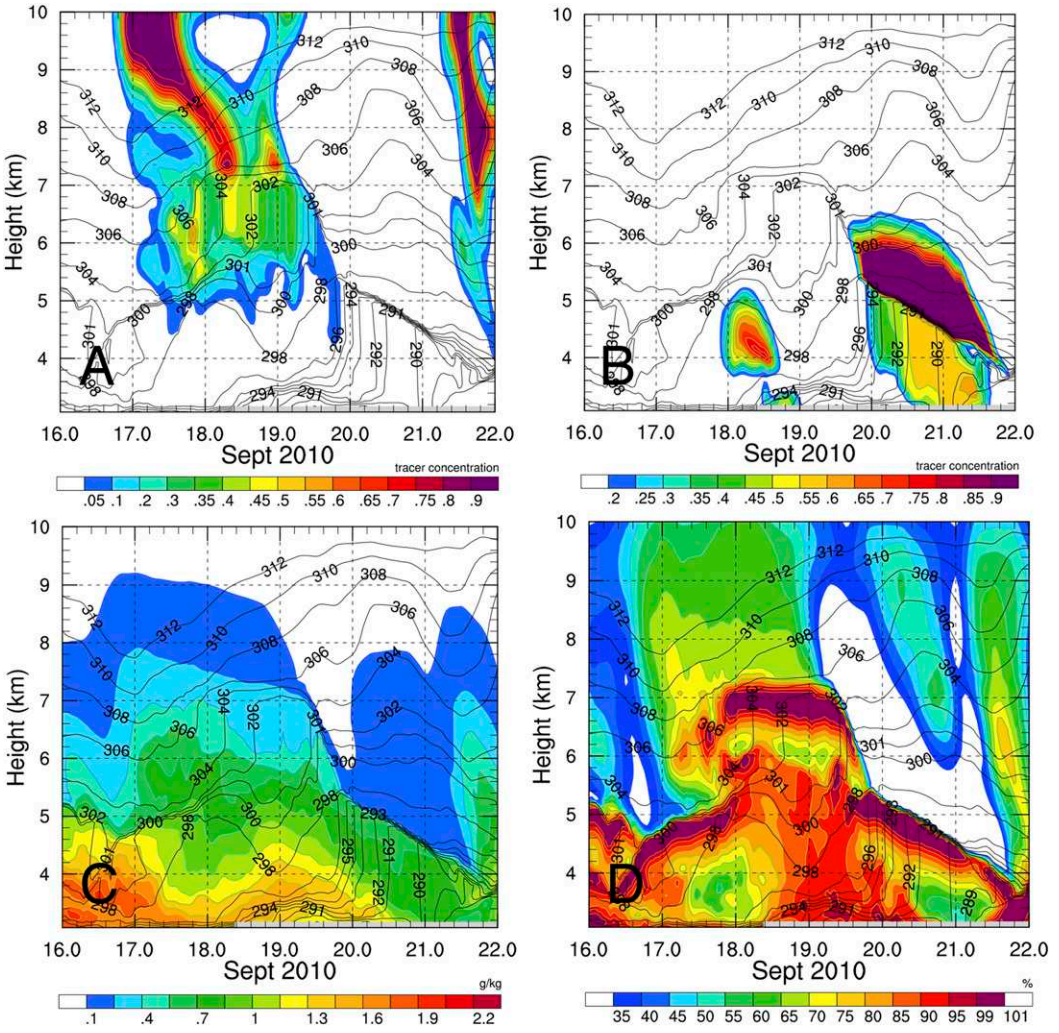

FIG. 8. Time–height cross sections of at Summit. (a) Tracer from south Greenland for MSE greater than 308 K (see Fig. 6a), in units of tracer concentration. (b) Tracer from the northwest for MSE = 292–301 K (see Fig. 6b), in units of tracer concentration. (c) Water vapor mixing ratio (g kg^{-1}). (d) Relative humidity (%). Black contours are MSE. Tracers are initialized at 0000 UTC 14 Sep 2010. Height is with respect to sea level.

cloud ice water path by a factor of 3. This dramatic decrease in LWP reduces the elevated cloud-driven turbulence (shading Fig. 12c) and dries the lowest 3 km through increased vapor deposition (contours Fig. 12c). The reduction in cloud-top cooling and cloud-driven turbulence warms the air above 6 km and cools the air below, increasing the stratification of the elevated cloud-driven mixed layer and reducing the stratification at cloud top at approximately 7 km height between 0000 UTC 18 September and 1200 UTC 19 September (Fig. 12d). Also, the reduction in LWP causes less downward surface longwave radiation, which cools the surface by 1°C (not shown).

Interestingly, the significant changes to the atmospheric boundary layer by the high ice clouds have a limited, but nonnegligible, impact on the stratocumulus clouds that forms after ~1800 UTC 19 September. There is less than 5 g m^{-2} difference in LWP between the control run and the run without high ice clouds for the period 1800 UTC 19 September and 1800 UTC 20 September. This shows that the cooling due to the less turbulent elevated cloud-driven mixed layer and the drying due to increased vapor deposition have compensating effects on the stratocumulus cloud formation.

To understand how the high ice clouds affect the subsequent stratocumulus clouds, Fig. 13 shows hourly total tracer tendency for tracer from the northwest (Figs. 13a,b) and contributions from total advection (Figs. 13c,d) and total diffusion (boundary layer plus diffusive mixing; Figs. 13e,f) from both the control simulation (Figs. 13a,c,e)

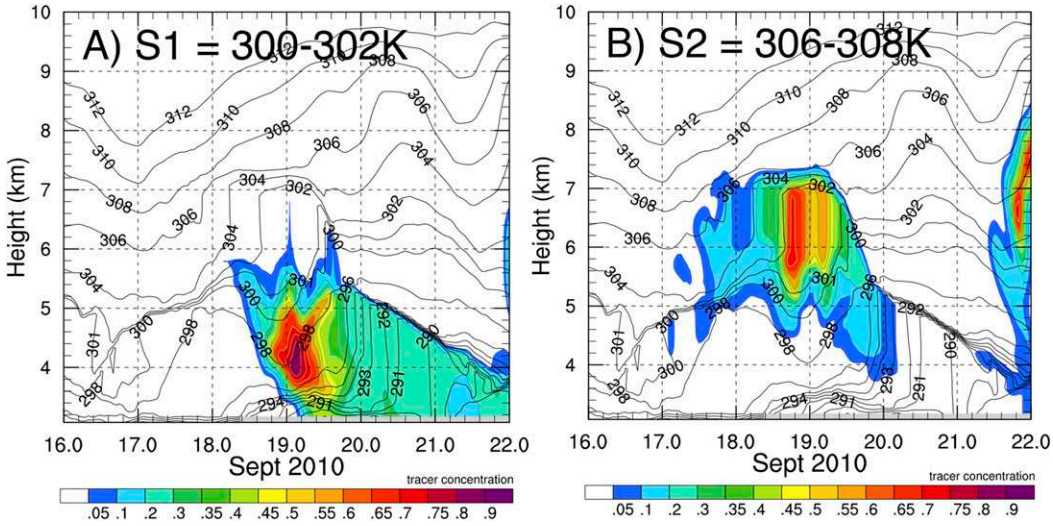

FIG. 9. Time–height cross-section at Summit of tracer concentration for tracer initialized in south Greenland with MSE intervals of (a) 300–302 K (tracer S1) and (b) 306–308 K (tracer S2), in units of tracer concentration. Black contours are MSE. Tracers are initialized at 0000 UTC 14 Sep 2010. Height is with respect to sea level.

and the sensitivity run (Figs. 13b,d,f). Figure 14 similarly shows the contribution to total advection from vertical advection (Figs. 13a,b) and horizontal advection (Figs. 13c,d) from both runs. The tracer that arrives at Summit at an elevation above 4 km initially has MSE greater than 294 K. Tracer tendencies in parcels with MSE less than 294 K indicate airmass modification due to radiative processes and turbulent mixing. The tracer tendencies (Figs. 13a,b) show that in the sensitivity simulation where high ice clouds are removed there is a large increase in tracer tendency at the start of stratocumulus period (0000 UTC 20 September) throughout the depth of the cloud-driven mixed layer, primarily due to horizontal advection (Figs. 13b and 14d). This is not seen in the control run indicating that the stratocumulus layer forms earlier in the sensitivity simulation (Figs. 13a and 14a), indicating that the lack of upper-level ice in the sensitivity simulation leads to differences in upstream processes responsible for the formation of the stratocumulus layer.

Figures 13a and 13b show episodic increases in tracer concentration in both runs that extend from the inversion to below the cloud-driven mixed layer. The increase(decrease) in tracer tendency is associated with periods of more(less) rapid cooling and drying. As expected, diffusion mixes tracer from the inversion at cloud top into the mixed layer (Figs. 13e,f). This mixing is episodic and peaks after local maxima in cloud liquid water. This mixing is modulated by mesoscale circulation below the cloud layer. In addition, during periods of maximum cloud liquid water, turbulent entrainment can balance large-scale subsidence, reducing the rate at which the cloud top lowers (Fig. 13f). The source of the tracer below the mixed layer is due to episodic horizontal advection of tracer below the well-mixed layer (Figs. 14c,d), an indication of deeper cloud-driven mixing upstream, which is mixed into the mixed layer at Summit by resolved vertical advection (Figs. 14a,b). The tracer that mixes into the mixed layer at the mixed-layer base has MSE less than 294 K, which indicates that the air mass has been modified by longwave cooling and turbulent mixing. It is interesting to note that when the cloud-driven mixed layer becomes coupled to the surface layer after 1900 UTC 20 September, horizontal advection is negative from the surface to the top of the inversion, potentially due to the mixing of low tracer surface layer air into the mixed layer. The decrease of tracer on 20 September is larger in the sensitivity simulation than in the control run due to a strong updraft (greater than 4 cm s^{-1}) in the mixed layer, which increases vertical advection and causes the increase in tracer due to total advection to be less than the decrease in tracer due to total diffusion (Figs. 13d,f). This limits the entrainment of cold/dry air at cloud top that is potentially aerosol limited due to the northern source. Given the different sources of the air masses above and below the stratocumulus deck, it would be interesting to see how enhanced entrainment affects the cloud properties when prognostic aerosols are included.

5. Summary and conclusions

In this study we investigate cloud formation and transitions in cloud types at Summit, Greenland, during 16–22 September 2010, when a warm, moist air mass was

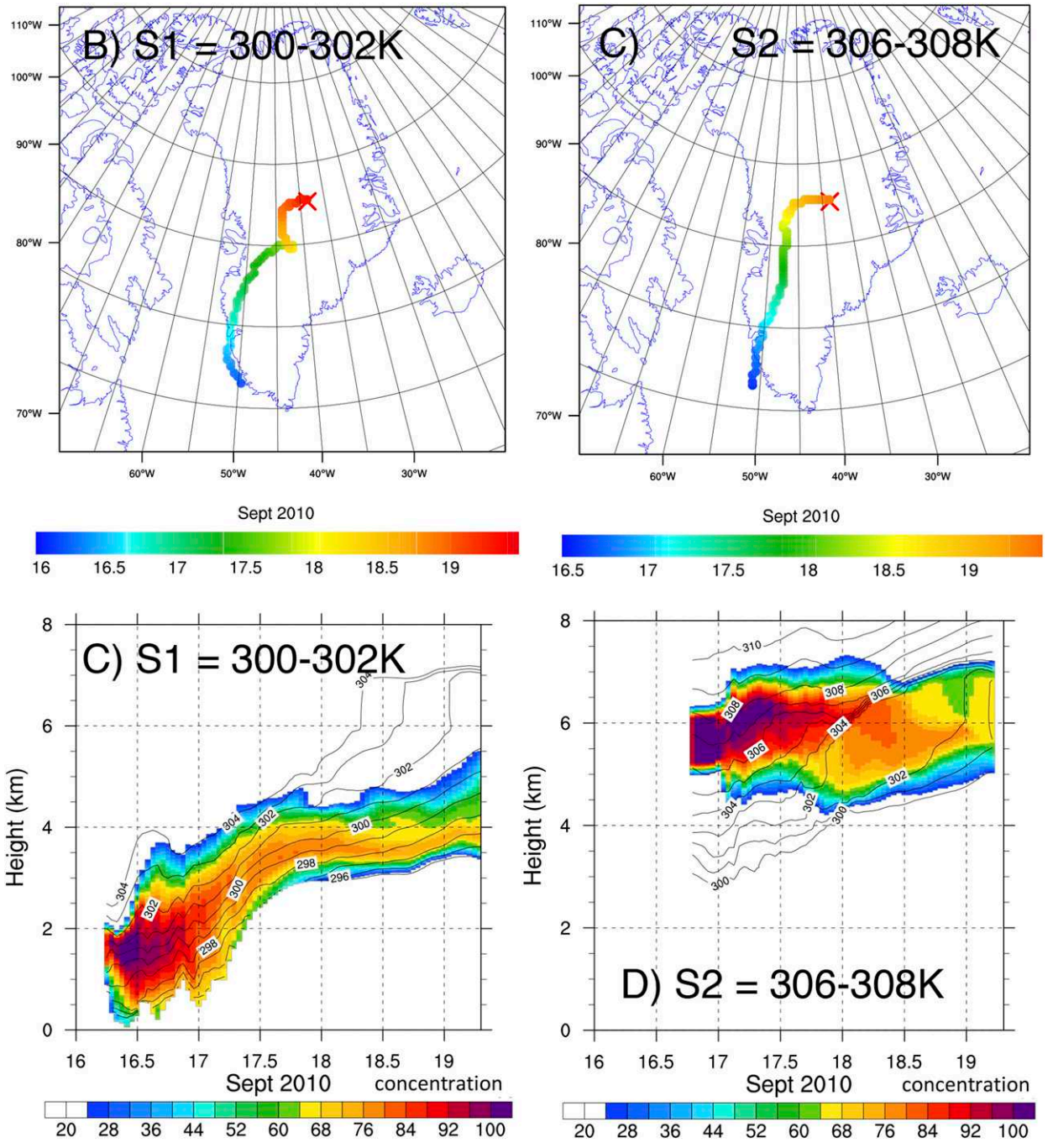

FIG. 10. (top) Trajectories to Summit for tracers (a) S1 and (b) S2. (bottom) Tracer concentrations (%) and MSE (K) along (c) S1 and (d) S2 trajectories. The tracer is advected south out of the domain before 16 Sep 2014.

advected to Greenland from lower latitudes. During this period there was a sharp transition between high ice clouds and the formation of a lower stratocumulus deck at Summit. The net surface radiative fluxes during the stratocumulus period are at least 20 $W m^{-2}$ larger than during the ice cloud period (Fig. 15), due to the close cancellation between upward and downward longwave fluxes when a cloud system radiates as a blackbody.

A tracer study is used to identify the origin of the air masses that form the ice and stratocumulus clouds and how they are modified as they are advected up over the Greenland Ice Sheet. When initialized at 0000 UTC 14 September 2010 we find essentially all the

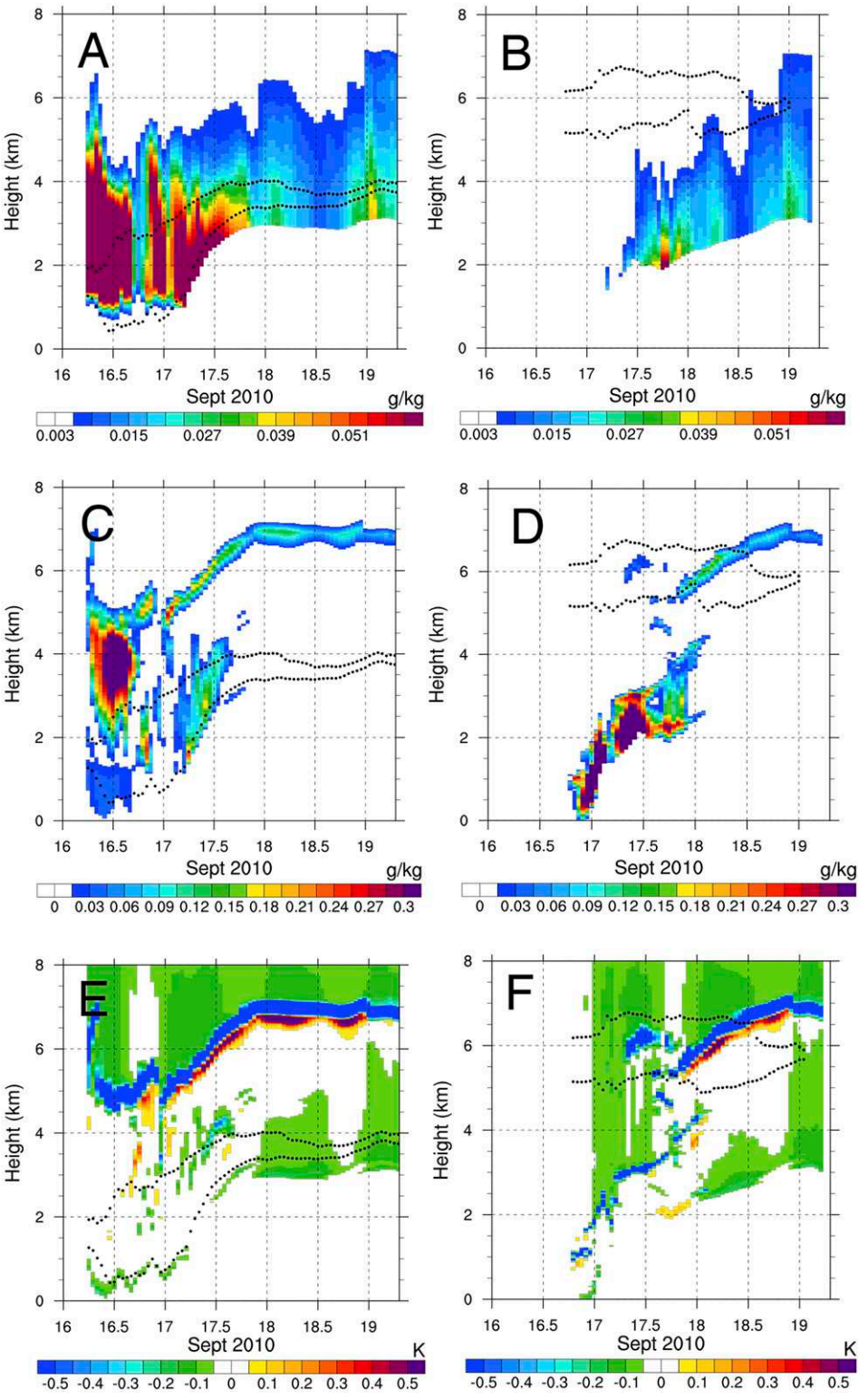

FIG. 11. Trajectories to Summit of (a),(b) ice water mixing ratio ($g\,kg^{-1}$), (c),(d) cloud liquid water mixing ratio ($g\,kg^{-1}$), and (e),(f) longwave plus shortwave radiative heating tendencies per hour (K) for tracer (a),(c),(e) S1 and (b),(d),(f) S2. The two black dotted lines mark the 70% tracer concentration lines. Height is with respect to sea level.

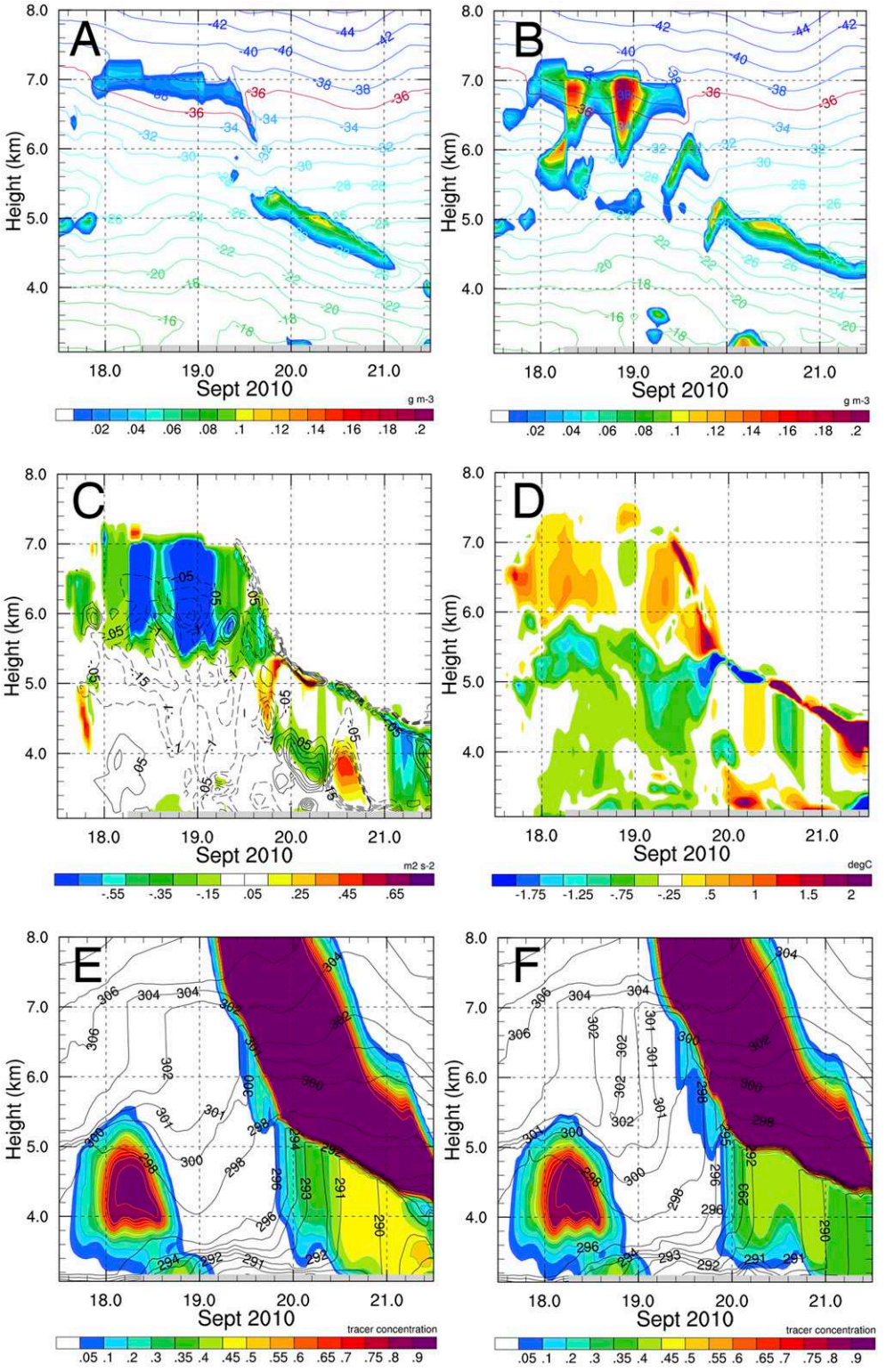

FIG. 12. Sensitivity of boundary layer and cloud properties to high ice clouds. (a) Cloud liquid water ($g\,m^{-3}$) from control run. (b) Cloud liquid water ($g\,m^{-3}$) from run with high ice clouds removed after 1200 UTC 17 Sep. (c) Impact of high ice clouds (i.e., control minus sensitivity study) on subgrid TKE (shading; $m^2\,s^{-2}$) and water vapor mixing ratio (contours, negative dashed; $g\,kg^{-1}$). (d) Impact of high ice clouds (i.e., control minus sensitivity study) on temperature (K). (e) Tracer from the northwest from control run. (f) Tracer from the northwest from run with high ice clouds removed.

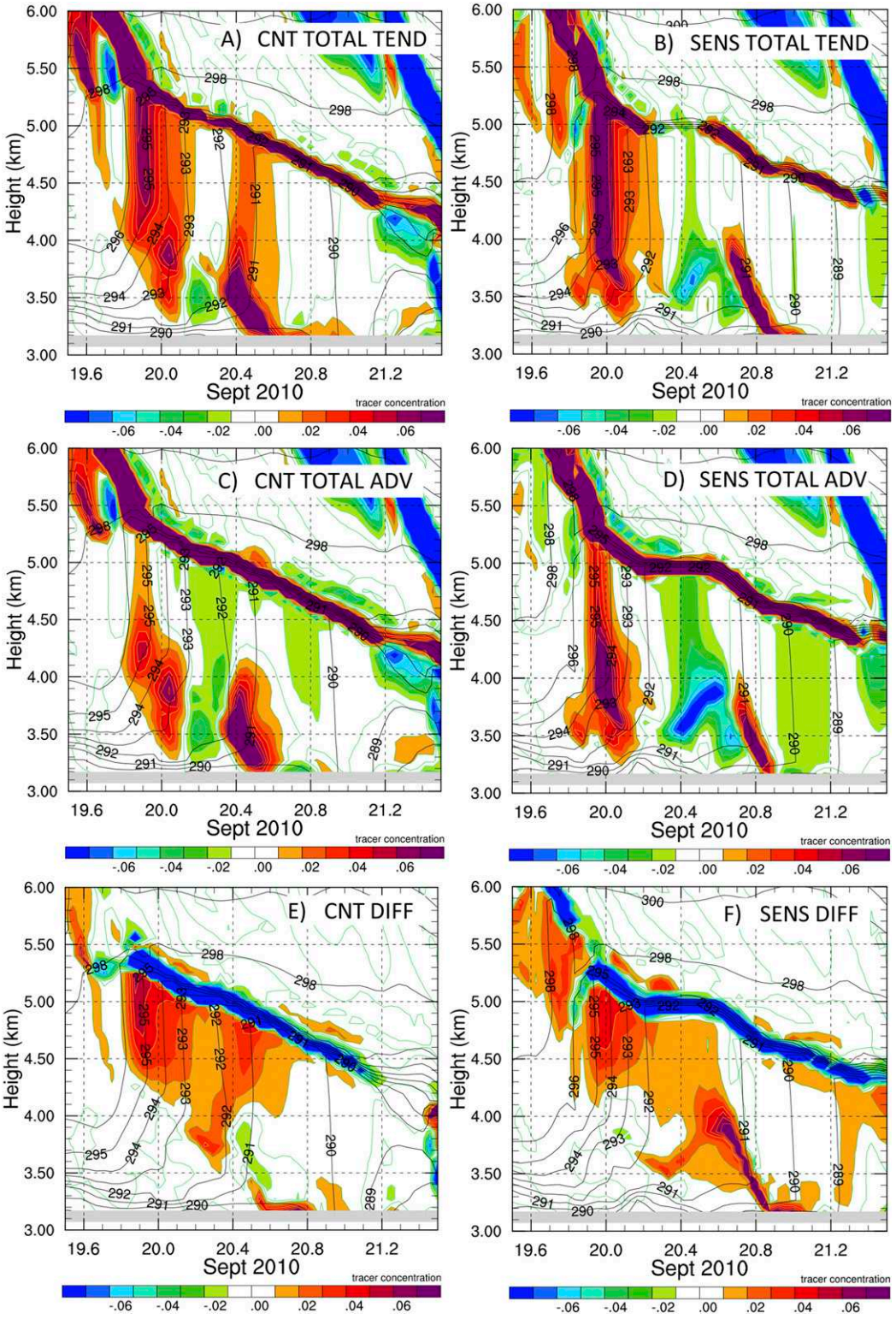

FIG. 13. Hourly tracer tendencies at Summit during the stratocumulus period (1200 UTC 19 Sep–1200 UTC 21 Sep) for tracer advected from the northwest coast of Greenland (see Fig. 5b) from both the control and sensitivity simulation. (a),(b) Total tracer tendency. (c),(d) Tracer tendency due to horizontal plus vertical advection. (e),(f) Tracer tendency due to diffusive mixing. (a),(c),(f) Tendencies from the control simulation. (b),(d),(e) Tendencies from the sensitivity simulation. Moist static energy (K) shown with black contours. Below ground level is indicated with gray shading.

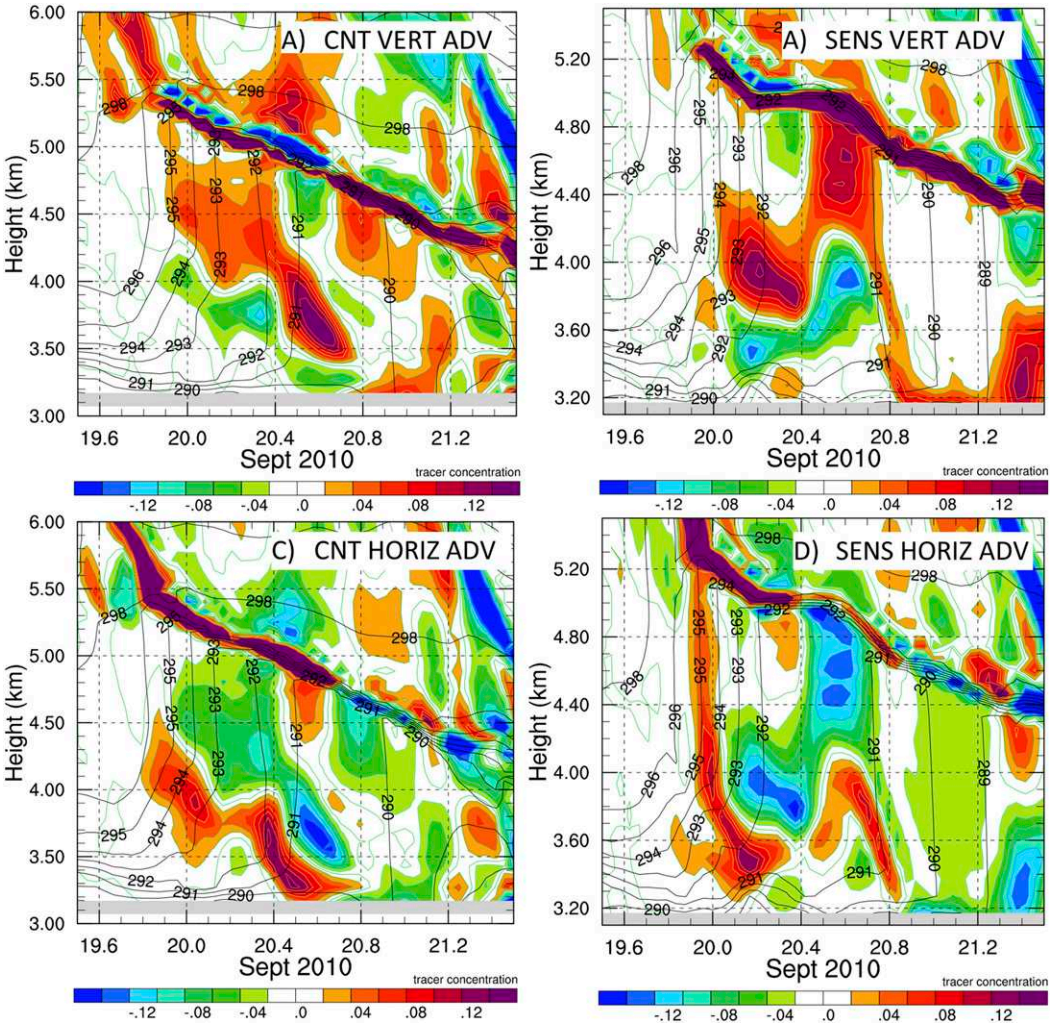

FIG. 14. Hourly tracer tendencies at Summit during the stratocumulus period (1200 UTC 19 Sep–1200 UTC 21 Sep) for tracer advected from the northwest coast of Greenland (see Fig. 5b) from both the control and sensitivity simulation. (a),(b) Tracer tendency due to vertical advection. (c),(d) Tracer tendency due to horizontal advection. (a),(c) Tendencies from the control simulation. (b),(d) Tendencies from the sensitivity simulation. Moist static energy (K) is shown with black contours. Below ground level is indicated with gray shading.

air that reaches Summit originates above the boundary layer and is advected in from outside the model domain. Based on the results from this case study we find that high ice clouds form when air masses are advected from the southwest Greenland coast at least 2 km above Summit. The MSE of this air decreases by ~4.5 K before reaching Summit due primarily to longwave radiative cooling, which causes ice formation due to homogeneous nucleation.

The mixed-phase stratocumuli form at the base of cold, dry air masses advected from the northwest overlying warm, moist air masses advected to Summit from the southwest 1–2 km above the boundary layer. Air masses from the northwest are entrained into the cloud-driven mixed layer at both the stratocumulus cloud top and the mixed-layer base. The air entrained at cloud top conserves MSE until it is mixed down into the Summit boundary layer through diffusive mixing, while the air masses at cloud base are modified by deeper mixed layers upstream. The air mass advected in from the southwest to the Summit boundary layer conserves MSE until it reaches the top of the GrIS, due to the saturated air mass aloft, which prevents the lower air mass from efficiently radiating to space.

A sensitivity study removing frozen hydrometeors that form above 5.5 km demonstrates that high ice clouds act to limit the formation of cloud liquid water, resulting in a less stable elevated cloud-driven mixed

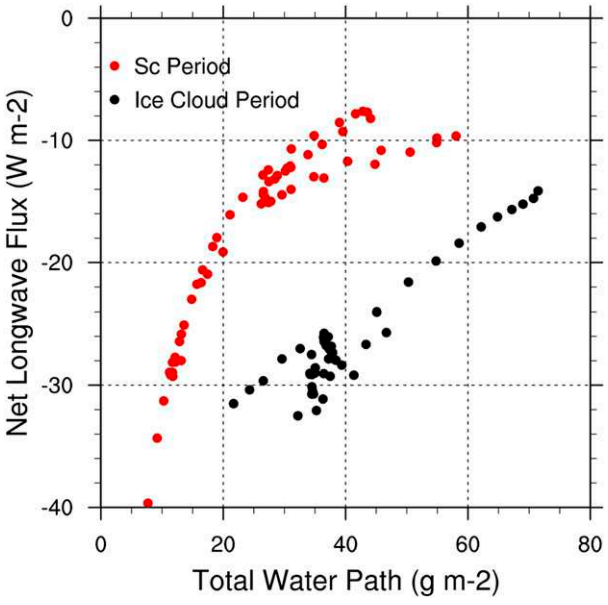

FIG. 15. The 30-min averaged total water path ($g\,m^{-2}$) and net surface longwave radiative flux ($W\,m^{-2}$) for the ice cloud (black) and stratocumulus periods (red). Note that the net radiative fluxes during the stratocumulus period are on average $20\,W\,m^{-2}$ larger than during the ice cloud period due to the close cancellation between upward and downward longwave fluxes when a cloud system radiates as a blackbody.

layer, a drying of the boundary layer through increased vapor deposition, and a cooling of the surface due to less downward surface longwave radiation. The cooling and drying of the boundary layer compensate to produce a limited impact on the stratocumulus cloud formation. The evolution of the cloud-driven boundary layer in both runs differs primarily due to mesoscale variability below the cloud layer, which can limit the entrainment of cold/dry and potentially aerosol-limited air advected to Summit from the northwest into the mixed layer. It would be interesting to see how variability in the entrainment of potentially aerosol-limited air masses advected from the northwest affects the cloud properties when prognostic aerosols are included.

Determining how moisture advection impacts cloud formation over the GrIS is critically important for understanding the net impact of clouds on the GrIS surface, and ultimately for projections of climate change. If moisture advection causes ice clouds to form instead of liquid or mixed-phase clouds this will have a dramatically different impact on the Greenland climate through differences in precipitation, radiative fluxes and cloud-driven mixing. Also, the results here suggest that ERA-Interim does not produce the correct cloud and boundary layer structure (likely related to difficulties in simulating liquid clouds), and thus likely does not correctly represent the airmass transformation processes explored in this paper. This deficiency could have wide-reaching implications for representations of the overall GrIS climate.

Summit is a nexus for cold, dry air masses advected in from the north and warm, moist air masses advected in from the south. The results of this study show the dependence of cloud formation at Summit on advection of warm, moist air masses from the south *and* cold, dry air masses from the northwest. During fall, warm, moist air masses advected into the central GrIS region from lower latitudes can cause ice clouds to form, which can actually limit the formation of cloud liquid water. Therefore, the results of this study suggest a mechanism whereby stratocumulus clouds that form at the base of cold, dry air masses can radiatively warm the top of the GrIS more effectively than moist air masses advected into the Greenland region from the south. To what extent this is a more general result outside of the summer season needs to be determined.

Acknowledgments. This research was supported by the National Science Foundation (PLR-1314156) and the NOAA Earth System Research Laboratory's Physical Science Division. Cloud and atmosphere observations were obtained from the NSF ICECAPS Project (OPP-1801477, 1801764, 1801318). Model forcing data sets were obtained from the European Centre for Medium-Range Weather Forecasts. We thank the numerous scientists and technicians responsible for obtaining and producing the observational and reanalysis data.

REFERENCES

Abdul-Razzak, H., and S. Ghan, 2000: A parameterization of aerosol activation: 2. Multiple aerosol types. *J. Geophys. Res.*, **105**, 6837–6844, https://doi.org/10.1029/1999JD901161.

Benedict, J. J., S. Lee, and S. B. Feldstein, 2004: Synoptic view of the North Atlantic Oscillation. *J. Atmos. Sci.*, **61**, 121–144, https://doi.org/10.1175/1520-0469(2004)061<0121:SVOTNA>2.0.CO;2.

Bennartz, R., and Coauthors, 2013: July 2012 Greenland melt extent enhanced by low-level liquid clouds. *Nature*, **496**, 83–86, https://doi.org/10.1038/nature12002.

Collins, W. D., and Coauthors, 2004: Description of the NCAR Community Atmosphere Model (CAM 3.0). NCAR Tech. Note NCAR/TN–464+STR, 214 pp.

Davini, P., C. Cagnazzo, R. Neale, and J. Tribbia, 2012: Coupling between Greenland blocking and the North Atlantic Oscillation pattern. *Geophys. Res. Lett.*, **39**, L14701, https://doi.org/10.1029/2012GL052315.

European Centre for Medium-Range Weather Forecasts, 2009: ERA-Interim Project (updated monthly). NCAR Computational and Information Systems Laboratory Research Data Archive, accessed 3 October 2018, https://doi.org/10.5065/D6CR5RD9.

Fang, Z.-F., 2004: Statistical relationship between the Northern Hemisphere sea ice and atmospheric circulation during winter

time. *Observation, Theory and Modeling of Atmospheric Variability*, X. Zhu et al., Eds., Meteorology of East Asia, Vol. 3, World Scientific, 131–141.

Franzke, C., S. Lee, and S. B. Feldstein, 2004: Is the North Atlantic Oscillation a breaking wave? *J. Atmos. Sci.*, **61**, 145–160, https://doi.org/10.1175/1520-0469(2004)061<0145:ITNAOA>2.0.CO;2.

Grenier, H., and C. S. Bretherton, 2001: A moist PBL parameterization for large-scale models and its application to subtropical cloud-topped marine boundary layers. *Mon. Wea. Rev.*, **129**, 357–377, https://doi.org/10.1175/1520-0493(2001)129<0357:AMPPFL>2.0.CO;2.

Häkkinen, S., D. K. Hall, C. A. Shuman, D. L. Worthen, and N. E. DiGirolamo, 2014: Greenland Ice Sheet melt from MODIS and associated atmospheric variability. *Geophys. Res. Lett.*, **41**, 1600–1607, https://doi.org/10.1002/2013GL059185.

Hall, R., R. Erdélyi, E. Hanna, J. M. Jones, and A. A. Scaife, 2015: Drivers of North Atlantic polar front jet stream variability. *Int. J. Climatol.*, **35**, 1697–1720, https://doi.org/10.1002/joc.4121.

Hanna, E., J. M. Jones, J. Cappelen, S. H. Mernild, L. Wood, K. Steffen, and P. Huybrechts, 2013: The influence of North Atlantic atmospheric and oceanic forcing effects on 1900–2010 Greenland summer climate and ice melt/runoff. *Int. J. Climatol.*, **33**, 862–880, https://doi.org/10.1002/joc.3475.

——, and Coauthors, 2014: Atmospheric and oceanic climate forcing of the exceptional Greenland Ice Sheet surface melt in summer 2012. *Int. J. Climatol.*, **34**, 1022–1037, https://doi.org/10.1002/joc.3743.

——, T. E. Cropper, P. D. Jones, A. A. Scaife, and R. Allan, 2015: Recent seasonal asymmetric changes in the NAO (a marked summer decline and increased winter variability) and associated changes in the AO and Greenland blocking index. *Int. J. Climatol.*, **35**, 2540–2554, https://doi.org/10.1002/joc.4157.

——, X. Fettweis, and R. J. Hall, 2018: Brief communication: Recent changes in summer Greenland blocking captured by none of the CMIP5 models. *Cryosphere*, **12**, 3287–3292, https://doi.org/10.5194/tc-12-3287-2018.

Hurrell, J., 1995: Decadal trends in the North Atlantic Oscillation: Regional temperatures and precipitation. *Science*, **269**, 676–679, https://doi.org/10.1126/science.269.5224.676.

Jimenez, P. A., J. Dudhia, J. F. Gonzalez–Rouco, J. Navarro, J. P. Montavez, and E. Garcia–Bustamante, 2012: A revised scheme for the WRF surface layer formulation. *Mon. Wea. Rev.*, **140**, 898–918, https://doi.org/10.1175/MWR-D-11-00056.1.

Klein, S. A., and Coauthors, 2009: Intercomparison of model simulations of mixed-phase clouds observed during the ARM Mixed-Phase Arctic Cloud Experiment. Part I: Single-layer cloud. *Quart. J. Roy. Meteor. Soc.*, **135**, 979–1002, https://doi.org/10.1002/qj.416.

Lawrence, D. M., and Coauthors, 2011: Parameterization improvements and functional and structural advances in version 4 of the Community Land Model. *J. Adv. Model. Earth Syst.*, **3**, M03001, https://doi.org/10.1029/2011MS00045.

Lim, Y.-K., S. D. Schubert, S. M. Nowicki, J. N. Lee, A. M. Molod, R. I. Cullather, B. Zhao, and I. Velicogna, 2016: Atmospheric summer teleconnections and Greenland Ice Sheet surface mass variations: Insights from MERRA-2. *Environ. Res. Lett.*, **11**, 024002, https://doi.org/10.1088/1748-9326/11/2/024002.

Moran, K., B. Martner, M. Post, R. Kropfli, D. Welsh, and K. Widener, 1998: An unattended cloud-profiling radar for use in climate research. *Bull. Amer. Meteor. Soc.*, **79**, 443–455, https://doi.org/10.1175/1520-0477(1998)079<0443:AUCPRF>2.0.CO;2.

Morrison, H., and J. O. Pinto, 2005: Mesoscale modeling of springtime Arctic mixed-phase stratiform clouds using a new two-moment bulk microphysics scheme. *J. Atmos. Sci.*, **62**, 3683–3704, https://doi.org/10.1175/JAS3564.1.

——, G. Thompson, and V. Tatarskii, 2009a: Impact of cloud microphysics on the development of trailing stratiform precipitation in a simulated squall line: Comparison of one- and two-moment schemes. *Mon. Wea. Rev.*, **137**, 991–1007, https://doi.org/10.1175/2008MWR2556.1.

——, and Coauthors, 2009b: Intercomparison of model simulations of mixed-phase clouds observed during the ARM Mixed-Phase Arctic Cloud Experiment. Part II: Multi-layered cloud. *Quart. J. Roy. Meteor. Soc.*, **135**, 1003–1019, https://doi.org/10.1002/qj.415.

Neff, W., G. Compo, F. M. Ralph, and M. D. Shupe, 2014: Continental heat anomalies and the extreme melting of the Greenland ice surface in 2013 and 1889. *J. Geophys. Res. Atmos.*, **119**, 6520–6536, https://doi.org/10.1002/2014JD021470.

Nghiem, S. V., and Coauthors, 2012: The extreme melt across the Greenland Ice Sheet in 2012. *Geophys. Res. Lett.*, **39**, L20502, https://doi.org/10.1029/2012GL053611.

Pedersen, R. A., I. Cvijanovic, P. L. Langen, and B. M. Vinther, 2016: The impact of regional Arctic sea ice loss on atmospheric circulation and the NAO. *J. Climate*, **29**, 889–902, https://doi.org/10.1175/JCLI-D-15-0315.1.

Shupe, M. D., 2007: A ground-based multisensor cloud phase classifier. *Geophys. Res. Lett.*, **34**, L22809, https://doi.org/10.1029/2007GL031008.

——, and Coauthors, 2013: High and dry: New observations of tropospheric and cloud properties above the Greenland Ice Sheet. *Bull. Amer. Meteor. Soc.*, **94**, 169–186, https://doi.org/10.1175/BAMS-D-11-00249.1.

Skamarock, W. C., and Coauthors, 2008: A description of the Advanced Research WRF version 3. NCAR Tech. Note NCAR/TN-475+STR, 113 pp., https://doi.org/10.5065/D68S4MVH.

Solomon, A., H. Morrison, P. O. G. Persson, M. D. Shupe, and J.-W. Bao, 2009: Investigation of microphysical parameterizations of snow and ice in Arctic clouds during M-PACE through model–observation comparisons. *Mon. Wea. Rev.*, **137**, 3110–3128, https://doi.org/10.1175/2009MWR2688.1.

——, M. D. Shupe, and N. B. Miller, 2017: Cloud–atmospheric boundary layer-surface interactions on the Greenland Ice Sheet during the July 2012 extreme melt event. *J. Climate*, **30**, 3237–3252, https://doi.org/10.1175/JCLI-D-16-0071.1.

Strong, C., and G. Magnusdottir, 2008: Tropospheric Rossby wave breaking and the NAO/NAM. *J. Atmos. Sci.*, **65**, 2861–2876, https://doi.org/10.1175/2008JAS2632.1.

Thompson, D. W. J., S. Lee, and M. P. Baldwin, 2002: Atmospheric processes governing the Northern Hemisphere Annular Mode/North Atlantic Oscillation. *The North Atlantic Oscillation: Climatic Significance and Environmental Impact*, *Geophys. Monogr.*, Vol. 134, Amer. Geophys. Union, 1–35.

Välisuo, I., T. Vihma, R. Pirazzini, and M. Schäfer, 2018: Interannual variability of atmospheric conditions and surface melt in Greenland in 2000–2014. *J. Geophys.*

Res. Atmos., **123**, 10 443–10 463, https://doi.org/10.1029/2018jd028445.

Vallis, G. K., and E. P. Gerber, 2008: Local and hemispheric dynamics of the North Atlantic Oscillation, annular patterns and the zonal index. *Dyn. Atmos. Oceans*, **44**, 184–212, https://doi.org/10.1016/j.dynatmoce.2007.04.003.

Walker, G., and E. Bliss, 1932: World weather V. *Mem. Roy. Meteor. Soc.*, **134**, 193–210.

Wallace, J., and D. Gutzler, 1981: Teleconnections in the geopotential height field during the Northern Hemisphere winter. *Mon. Wea. Rev.*, **109**, 784–812, https://doi.org/10.1175/1520-0493(1981)109<0784:TITGHF>2.0.CO;2.

Woollings, T., B. Hoskins, M. Blackburn, and P. Berrisford, 2008: A new Rossby wave breaking interpretation of the North Atlantic Oscillation. *J. Atmos. Sci.*, **65**, 609–626, https://doi.org/10.1175/2007JAS2347.1.

——, A. Hannachi, and B. Hoskins, 2010: Variability of the North Atlantic eddy-driven jet stream. *Quart. J. Roy. Meteor. Soc.*, **136**, 856–868, https://doi.org/10.1002/qj.625.